



HAL
open science

Simple Patient-Based Transmantle Pressure and Shear Estimate From Cine Phase-Contrast MRI in Cerebral Aqueduct

Gérald Bardan, Franck Plouraboué, Mokhtar Zagzoule, Olivier Balédent

► **To cite this version:**

Gérald Bardan, Franck Plouraboué, Mokhtar Zagzoule, Olivier Balédent. Simple Patient-Based Transmantle Pressure and Shear Estimate From Cine Phase-Contrast MRI in Cerebral Aqueduct. IEEE Transactions on Biomedical Engineering, 2012, vol. 59, pp.2874-2883. 10.1109/TBME.2012.2210716 . hal-00746487

HAL Id: hal-00746487

<https://hal.science/hal-00746487>

Submitted on 29 Oct 2012

HAL is a multi-disciplinary open access archive for the deposit and dissemination of scientific research documents, whether they are published or not. The documents may come from teaching and research institutions in France or abroad, or from public or private research centers.

L'archive ouverte pluridisciplinaire **HAL**, est destinée au dépôt et à la diffusion de documents scientifiques de niveau recherche, publiés ou non, émanant des établissements d'enseignement et de recherche français ou étrangers, des laboratoires publics ou privés.



Open Archive TOULOUSE Archive Ouverte (OATAO)

OATAO is an open access repository that collects the work of Toulouse researchers and makes it freely available over the web where possible.

This is an author-deposited version published in : <http://oatao.univ-toulouse.fr/>
Eprints ID : 6643

To link to this document : DOI:10.1109/TBME.2012.2210716
URL : <http://dx.doi.org/10.1109/TBME.2012.2210716>

To cite this version : Bardan, Gérald and Plouraboué, Franck and Zagzoule, Mokhtar and Baledent, Olivier
Simple Patient-Based Transmantle Pressure and Shear Estimate From Cine Phase-Contrast MRI in Cerebral Aqueduct. (2012) IEEE Transactions on Biomedical Engineering, vol. 59 (n° 10). pp. 2874-2883. ISSN 0018-9294

Any correspondance concerning this service should be sent to the repository administrator: staff-oatao@inp-toulouse.fr.

Simple Patient-Based Transmantle Pressure and Shear Estimate From Cine Phase-Contrast MRI in Cerebral Aqueduct

Gérald Bardan*, Franck Plouraboué, Mokhtar Zagzoule, and Olivier Balédent

*G. Bardan is with the Institute of Fluid Mechanics of Toulouse, UMR, University of Toulouse, 5502 Toulouse, France (e-mail: gbardan@imft.fr).

F. Plouraboué and M. Zagzoule are with the Institute of Fluid Mechanics of Toulouse, UMR, University of Toulouse, 5502 Toulouse, France (e-mail: fplourab@imft.fr; zagzoule@cict.fr).

O. Balédent is with the Centre Hospitalier Universitaire Amiens, 80054 Amiens, France (e-mail: Olivier.Baledent@chu-amiens.fr).

Abstract—From measurements of the oscillating flux of the cerebrospinal fluid (CSF) in the aqueduct of Sylvius, we elaborate a patient-based methodology for transmantle pressure (TRP) and shear evaluation. High-resolution anatomical magnetic resonance imaging first permits a precise 3-D anatomical digitalized reconstruction of the Sylvius’s aqueduct shape. From this, a very fast approximate numerical flow computation, nevertheless consistent with analytical predictions, is developed. Our approach includes the main contributions of inertial effects coming from the pulsatile flow and curvature effects associated with the aqueduct bending. Integrating the pressure along the aqueduct longitudinal center line enables the total dynamic hydraulic admittances of the aqueduct to be evaluated, which is the pre-eminent contribution to the CSF pressure difference between the lateral ventricles and the subarachnoid spaces also called the TRP. The application of the method to 20 healthy human patients validates the hypothesis of the proposed approach and provides a first database for normal aqueduct CSF flow. Finally, the implications of our results for modeling and evaluating intracranial cerebral pressure are discussed.

Index Terms—Aqueduct of Sylvius, cerebrospinal fluid (CSF), electric impedance modeling, Fourier decomposition, intracranial pressure, pulsatile flows, transmantle pressure (TRP).

I. INTRODUCTION

MAGNETIC resonance imaging (MRI) and cine phase-contrast allow accurate anatomical imaging and specific valuation of pulsation velocities and fluxes inside brain cavities and vessels. It is now an invaluable tool for investigations in physiology and pathology [1]–[3]. Electric models have been proposed to describe hydraulic couplings between various intracerebral spaces (e.g., subarachnoid spaces (SAS), ventricular spaces, and intrathecal spaces of the spinal canal) [4]–[8]. Recent contributions also point out that patient-based flux and

pressure measurements can be found from control volume compartmental image analysis and could contribute to a better understanding of intracranial dynamics and progression to disorder [9]. Furthermore, since some *in vivo* measurements are possible, it is tempting to use computational fluid dynamics (CFD) for a deeper understanding of the cerebrospinal fluid (CSF) flow [10]–[12], and for a better description of the CSF pressure variations inside the brain as well as a more complete understanding of the hydraulic coupling within the various intracerebral compartments. However, even though numerical computations have already been developed for CSF flow inside the third or fourth ventricles [11], it should be borne in mind that complete computations of CSF flow fields inside brain cavities have to face difficult obstacles, if not challenges.

First, the numerical evaluation of temporally oscillating flows inside very complex cavity shapes is a 4-D problem that needs massive data storage and heavy and lengthy computations, the precision of which is difficult to control. It is important to realize that, since the size of the smallest (e.g., intrathecal space and Sylvius aqueduct) and largest cavities (ventricles) differ by a large factor and adaptive mesh is necessary. This involves various issues such as mesh generation, regularization, and refinement, the quality of which necessitates much effort and case-specific treatments. CSF is mainly produced by the choroid plexus of the lateral ventricle (LV) and it is mainly reabsorbed by the Paccioni granulation pathway in the venous blood through the sagittal Sinus [13], [14]. Under normal circumstances, CSF oscillates in and out of the ventricular system with a net outward flow Q_s equal to the physiological production rate of CSF. The aqueduct, a slightly curved pipe with a variable elliptic section, is the smallest cavity between the LV and SAS. This is where most of the viscous dissipation, and thus most of the pressure drop, occurs as illustrated in [12], Fig. 5]. The pressure in large cavities is found to be spatially uniform while most variation occurs within the cerebral aqueduct. Pressure variations inside the third ventricle are typically smaller than 0.5 Pa [11], while transmantle pressure (TRP) is close to 4 Pa [12]. The aqueduct influence thus deserves special attention, especially in stenotic conditions [5], [15]. In the field of fluid mechanics, oscillating pulsed flow in curved pipes has received considerable attention [16]–[18]. It involves three independent parameters: 1) the ratio between the typical radius R of the pipe and its radius of curvature R_c , $\lambda = R/R_c$; 2) the product between viscous diffusion time and the main cardiac forcing pulsation ω described by the so-called Womersley number $\alpha^2 = \omega \rho R^2 / \mu$, where ρ and μ are, respectively, the

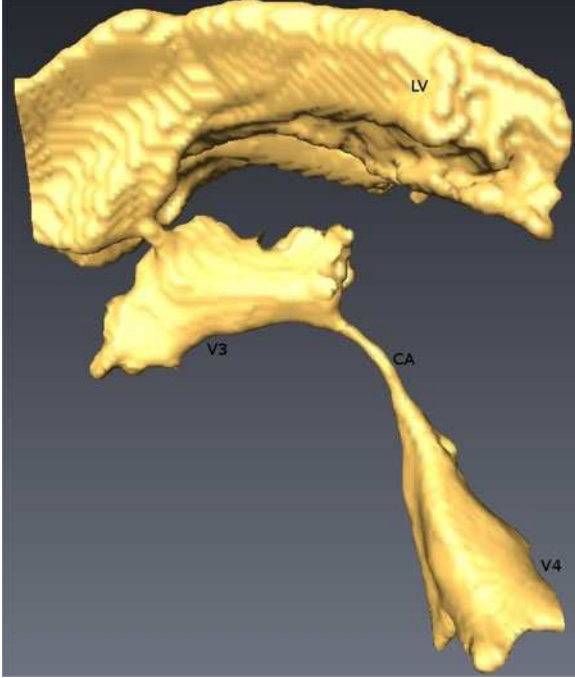


Fig. 1. Example of cerebral aqueduct (CA) joining the third (V3) and fourth (V4) ventricle visualized from a volume rendering in the sagittal plane of the anatomical MRI image of patient A. LVs can be seen on top.

density and dynamic viscosity of the CSF (very close to water), 3) the Reynolds number $Re = \rho U \bar{a} / \mu$, where U is the averaged longitudinal velocity inside the aqueduct and \bar{a} is the mean cross-sectional ellipse's major axis averaged along the aqueduct centerline, which is approximated by the average over all major axis a_i of ellipses Ω_i in all sections i (see Fig. 2), i.e., $\bar{a} = (1/L) \int_0^L a(s) ds \simeq (1/n) \sum_{i=1}^n a_i$. The average longitudinal velocity $U = Q / \pi \bar{a} \bar{b}$ is defined as the measured flux (which is constant along the aqueduct) over the average section $\pi \bar{a} \bar{b}$, where, again, \bar{b} is the average ellipse Ω_i minor axis in each section i . Usually, two supplementary parameters, which are a combination of the above, are also considered: the Dean number $De = Re \cdot \sqrt{\lambda}$ and the reduced Reynolds number $Re_s = (Re/\alpha)^2 \lambda$. Depending on the value of these parameters, some complex flow patterns and case-specific approximations can be built [16]–[20]. Since the physiological Womersley number α typically lies between 5 and 30, the flow field variations inside the cavities are generically localized in the vicinity of the walls, within so-called Stokes layers. These layers can be either large or small, so a finer grid discretization is also needed inside them if velocity is to be evaluated properly. We show below that the Stokes layers develop around 10% of the radius (mean value of the Womersley number in Table II).

Finally, from the acquisition point of view, as pointed in [12], it is difficult to obtain anatomically reliable data for the smallest cavities (e.g. SAS and intrathecal spaces) and the mechanical parameters used to describe soft tissue deformations and poroelastic behaviors. For all these reasons, it is interesting to develop alternative approaches to full CFD, such as [12], for CSF modeling and case-specific analysis. Such alternative approaches are

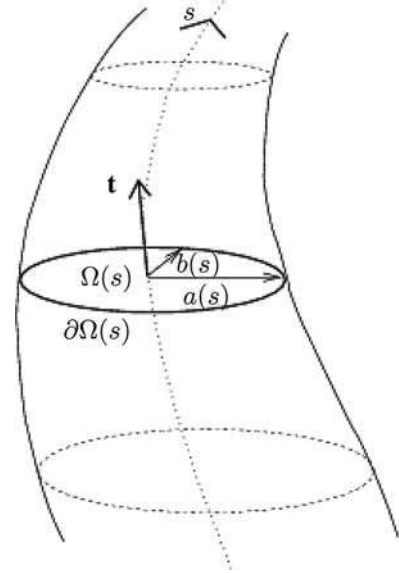


Fig. 2. Sketch of the cerebral aqueduct centerline description with associated transverse elliptic section $\Omega(s)$ having minor axis $b(s)$, major axis $a(s)$, and ellipse frontier $\partial\Omega(s)$ at longitudinal curvilinear distance s .

not always possible: they depend on the geometry involved and on the flow conditions.

In this paper, we show that a slightly curved aqueduct of Sylvius with low reduced Reynolds number is a fair description that leads to a fast estimation of the pressure drop, shear, and hydraulic admittance. This analysis provides an equivalent frequency-dependent electric impedance description of the TRP/flux relationship, and is, to our knowledge, the first explicit evaluation available in a healthy cohort of patients. Section II describes the four-step method [aqueduct reconstruction (see Section II-A), fluid flow (see Section II-B), Fourier decomposition and hydraulic admittances (see Section II-C), and physiological validation of the model hypothesis (see Section II-D)] that we put forward here associated with asymptotic evaluation of the aqueduct of Sylvius hydraulic admittances. Section III shows the evaluation of these hydraulic admittances for three out of 20 real patients, resulting from the first Fourier modes decomposition of their cardiac cycle variations. We, finally, discuss the relevance of the results obtained for the derivating realistic electrical models of complete CSF hydraulic models in Section III.

II. METHODS

A. Aqueduct Reconstruction

MRI acquisitions were obtained using the method described in [1] and [21] with isotropic voxels of $\Delta x = \Delta y = \Delta z = 0.55$ mm. The anatomical orientation of the aqueduct is sagittal and mostly vertical. Thus, it was possible to obtain a reliable 3-D digitalized reconstruction of it by analyzing each successive horizontal section (cf., Fig. 2). In each horizontal section, we extracted the elliptical contour that best fitted the gray-level anatomical image of the aqueduct (cf., Fig. 3). First, we drew (dotted line) a contour plot of the gray-scale image with equally

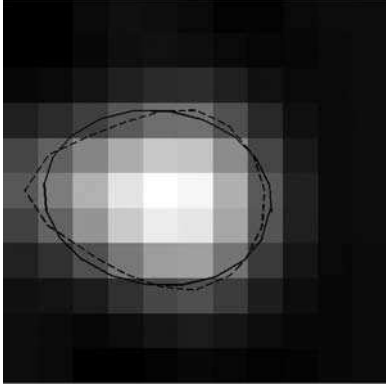


Fig. 3. Gray-level anatomical slice of the aqueduct. Dotted line: gray-level contour profile of the aqueduct. Continuous line: ellipse extracted from best fit of the contour line (Patient A).

spaced contour levels in the plot. Then, in the least squares sense, we plotted (continuous line) the best fit ellipse. For each ellipse, the center, major radius $a(s)$, and minor radius $b(s)$ were extracted. From the evaluation of the ellipse's center in each successive horizontal section, the aqueduct centerline was reconstructed. Over the human patients examined, we found that, to a good approximation, this centerline lies within the sagittal plane. Hence, it was easy to evaluate the main radius of curvature of the resulting planar centerline curve. Using a quadratic minimization among the discrete set of n points of the centerline, it was possible to extract the main radius of curvature R_c of the aqueduct centerline, which quantified its bending in the sagittal plane as well as the curvilinear length L of the centerline. For some patients, a double bending of the centerline was observed, with two radii of curvature of opposite sign (cf., Fig. 4). In this case, each radius of curvature R_{c+} (respectively, R_{c-}) was fitted using a properly chosen number of points n_+ (respectively, n_-) among the total number of points $n = n_+ + n_-$, giving less than 5% relative difference with the centerline in every case. The average curvature was thus computed from

$$R_c = \frac{n_+ R_{c+} + n_- R_{c-}}{n}, \quad \lambda = \frac{\bar{a}}{R_c} \quad (1)$$

where the influence of curvature on the CSF flow can be quantified by the dimensionless parameter λ . Here, again, \bar{a} is the longitudinally averaged major axis of the elliptical cross section of the aqueduct over cross-sectional images, i.e., $\bar{a} = (1/L) \int_0^L a(s) ds \simeq (1/n) \sum_{i=1}^n a_i$. Other useful parameters, of interest, for quantitative comparison with previous analyses [19], [20], were also derived from the major and minor radii a and b , such as the mean eccentricity \bar{e} and the mean ellipticity \bar{m} , defined as

$$\bar{e} = \sqrt{1 - \frac{b^2}{a^2}}, \quad \bar{m} = \sqrt{\frac{a-b}{a+b}}. \quad (2)$$

The values observed for parameter \bar{m} ($\bar{m} \simeq 0.6$, as seen in Fig. 5 and Table II) showed that slightly noncircular models of the cerebral aqueduct were not relevant, and called for fully elliptic cross sections geometries. Also, a Fourier mode

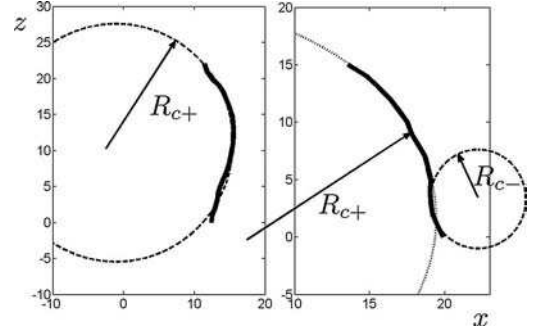


Fig. 4. Result of centerline segmentation in the sagittal plane (unit in voxel = 0.55 mm). Radius of curvature R_c fitting in two cases for $n_+ = n$ and $n_- = 0$ (left, Patient B) and for $n_+ = \frac{7n}{10}$ and $n_- = \frac{3n}{10}$ (right, Patient C).

decomposition of the flow rate during the cardiac cycle, similar to [22], is proposed in the next sections.

B. Fluid Flow, Pressure, and Shear Evaluation Within the Aqueducts

In this section, we use an asymptotic approach for flow evaluation. This model is derived from an asymptotic approximation of the Navier–Stokes equations without considering elastic deformation, consistently with [18]–[20]. It is necessary to consider a dimensionless formulation of the problem, which can then provide a patient-independent formulation whatever the particular aqueduct shape or cardiac temporal forcing. Taking * for dimensional quantities, let us first discuss a formulation for curvilinear coordinates, s , associated with the centerline arc length following [18]. Since the aqueduct is slightly bent, s is nondimensionalized by the radius of curvature R_c , $s^* = R_c s$, while the radial coordinate $r^* = \bar{a} r$ is nondimensionalized by the typical transverse length \bar{a} . The forcing pulsation is used to define dimensionless time $t^* = t/\omega$, where the typical longitudinal velocity provides the scaling for the longitudinal velocity component $u^* = U u$. A viscous pressure is used for the pressure nondimensionalization since we consider moderate reduced Reynolds numbers, as will be seen in Section II-D, so that $p^* = (\mu U L / \bar{a}^2) p$. The dimensionless flux is defined by $Q^* = U \bar{a}^2 Q$, where Q^* is given by MRI acquisitions. Following previous authors and seeking the leading order, slightly curved, low Reynolds number flow description, the longitudinal velocity component forced by a single sinusoidal mode forcing with associated local longitudinal pressure gradient $\frac{\partial p}{\partial s}(s)$ satisfies

$$\nabla^2 u - \alpha^2 \frac{\partial u}{\partial t} = -\frac{\partial p}{\partial s} \quad (3)$$

where ∇^2 is the Laplacian operator in the plane locally orthogonal to the centerline at curvilinear distance s , to be solved with boundary condition $u = 0$ on the frontier $\partial\Omega(s)$ of the local transverse elliptic section $\Omega(s)$ having major and minor radii $a(s)$ and $b(s)$. The local pressure gradient is decomposed into a stationary $K_S(s)$ and unstationary $K_U(s)$. In subsequent notations, index S (respectively, U) is associated with stationary

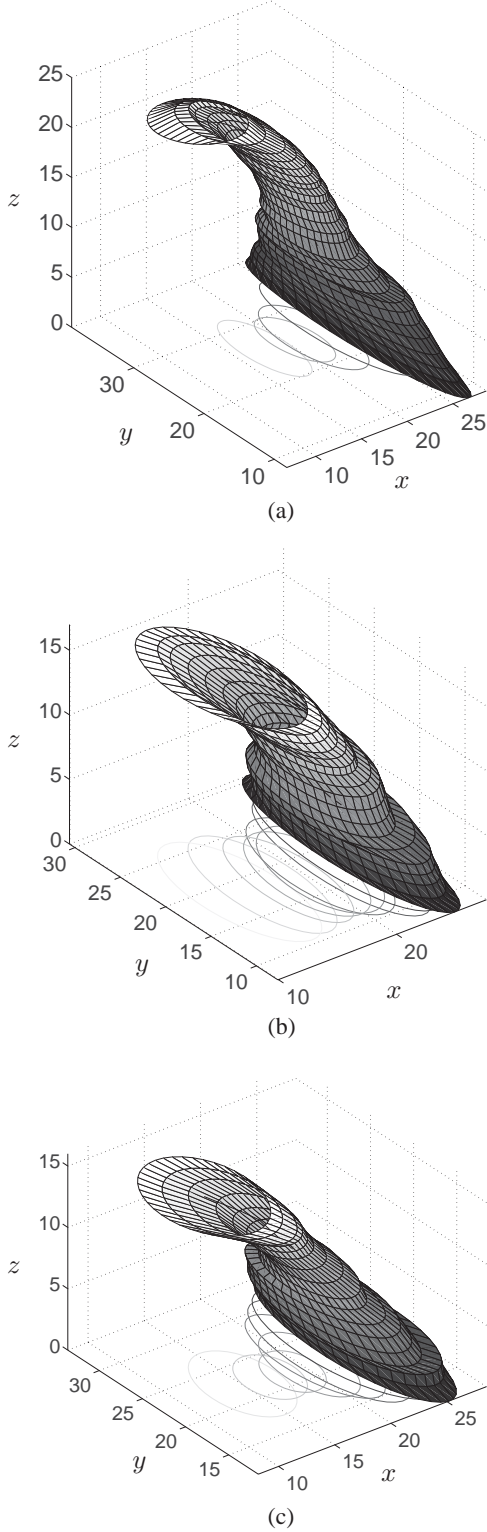


Fig. 5. Reconstructed aqueduct for three healthy patients anonymized as Patient D, Patient E, and Patient F.

(respectively, unstationary) cases

$$\frac{\partial p}{\partial s} = K_S(s) + \Re(K_U(s)e^{it}). \quad (4)$$

1) *Stationary forcing*: Solving (3) for $\alpha = 0$ and $\frac{\partial P}{\partial s} = K_S(s)$ leads to

$$u_S(x, y, s) = -\frac{1}{2} \frac{a^2 b^2}{a^2 + b^2} \left(1 - \frac{x^2}{a^2} - \frac{y^2}{b^2}\right) K_S(s) \quad (5)$$

in the coordinates x, y locally orthogonal to the centerline arc length s , oriented toward the principal axis of the ellipse $\Omega(s)$ (see Fig. 2). The associated longitudinal flux $Q_S = \int_{\Omega} u_S dS$ with infinitesimal elementary surface $dS = dx dy$ in Ω_i reads

$$Q_S = -y_S(s) K_S(s) \quad (6)$$

where we have introduced the local complex hydraulic admittance of the stationary contribution $y_S(s) = C_S(s) + iS_{cS}(s)$ which is, in this case, a pure real conductance

$$y_S(s) = C_S(s) = \frac{\pi}{4} \frac{a^3 b^3}{a^2 + b^2} \quad (7)$$

since, for nonoscillating flow, the imaginary hydraulic susceptance contribution is zero, $S_{cS}(s) = 0$. The local pressure gradient $K_S(s)$ is adapted so that constant flux is preserved in each successive section Q_S . By considering the leading order contribution to the viscous stress tensor of this longitudinally dominated flow, we also evaluate the shear stress τ_S . It can be expressed (see the Appendix) at leading order $O(\lambda)$ in the coordinates locally orthogonal to the centerline arc length s , in the principal axis coordinates of the ellipse $\Omega(s)$, along its frontier $\partial\Omega(s)$

$$\tau_S = \lambda \frac{a^2 b^2}{a^2 + b^2} \sqrt{\frac{x^2}{a^4} + \frac{y^2}{b^4}} K_S(s) \quad (8)$$

where index s refers to stationary flow contribution and \mathbf{t} is the local tangent vector to the centerline at location s . By integrating around the elliptic contour $\partial\Omega(s)$, we can see that the simple result for the leading order total shear at the wall $\tau_{TS} = \int_{\partial\Omega} \tau_S dl$ is

$$\tau_{TS}(s) = -\lambda \pi ab K_S(s). \quad (9)$$

2) *Unstationary forcing*: Solving (3) for nonzero α with complex velocity u_U and forcing $\frac{\partial P}{\partial s} = K_U(s)e^{it}$ is performed numerically using a finite-element discretization of $\Omega(s)$ with a classical variational formulation using $P0$ elements [23]. From the numerical evaluation of the complex velocity component u_U , the flux Q_U can be computed numerically from a simple spatial integration $Q_U = \int_{\Omega} u_U dS$. On the other hand, Haslam and Zamir [24] provide an analytical expression for the flux

$$Q_U = -\Re(y_U(s) K_U(s)e^{it}) \quad (10)$$

which can be expressed using the local complex admittance $y_U(s)$:

$$y_U(s) = \frac{2\pi i}{\eta} \frac{a^3 b^3}{a^2 + b^2} \left(1 - \frac{2J_1(\sqrt{-i\eta})}{\sqrt{-i\eta} J_0(\sqrt{-i\eta})}\right) \quad (11)$$

with $\eta = 2 \frac{a^2 b^2}{a^2 + b^2} \alpha^2$ and J_0, J_1 the zeroth- and first-order Bessel functions. Consistently with previous results (11) tends to (7) as $\alpha \rightarrow 0$. The analytical result (11) (derived from [24]) is fully consistent with finite-element numerical evaluation, as represented in Fig. 10.

TABLE I
INFLUENCE OF THE FOURIER MODE TRUNCATION ON THE RECONSTRUCTED FLUX (PATIENT D)

n	1	2	3	4	5	6
E_n	0.31	0.12	0.06	0.05	0.03	0.02

Similar to the stationary case, the oscillating part of the shear leading order wall shear stress is approximately given by (see the Appendix)

$$\tau_U = -\lambda \Re \left(\int_{\Omega} (K_U(s) - i\alpha^2 u_U) dS e^{it} \right) \quad (12)$$

or, using the flux expressions (10) and (11)

$$\tau_U = -\lambda \pi a b \Re \left(\frac{2J_1(\sqrt{-i\eta})}{\sqrt{-i\eta} J_0(\sqrt{-i\eta})} e^{it} \right) K_U(s) \quad (13)$$

which obviously tends to (9) as $\alpha \rightarrow 0$ and $\eta \rightarrow 0$.

C. Fourier Decomposition and Hydraulic Admittances

1) *Fourier Decomposition of the Flux*: The experimental flux is decomposed into discrete Fourier modes from a signal having 32 points per cardiac cycle. The zeroth mode corresponds to the stationary flux Q_S . The constant flux amplitude is generally smaller than the first oscillatory mode by almost three orders of magnitude. It is thus difficult to obtain a reliable Fourier decomposition, and this is why a dedicated acquisition sequence has previously been proposed for its evaluation [10], [25]. From the $f^k = \frac{2\pi}{\omega^k}$ frequency, we compute the sequence of Womersley numbers α^k for which the admittance $y_U^k(s)$ is evaluated for a flux amplitude $Q_U^k(t)$. A truncated reconstruction of the variation of the flux $Q_n(t) = \sum_0^n Q_U^k(t)$ over the complete cardiac cycle $[0, T_c]$ taking only the first n modes has been tested. The L^2 norm error E_n recovered from the truncated evaluation is

$$E_n = \sqrt{\frac{\int_0^{T_c} (Q_{\text{exp}} - Q_n)^2 dt}{\int_0^{T_c} (Q_{\text{exp}})^2 dt}}.$$

It is represented in Table I and Fig. 6. This computation shows that keeping only the first three modes provides an accurate description to within 10% of the flux temporal variation. The saturation of the error for $n > 3$ arises since there is a modest number of points per cycle (32 here).

2) *Hydraulic Admittances and TRP Reconstruction*: Equations (6) and (10) describe a local linear relation between the flux and the pressure gradient associated with a local admittance. The local admittance is also the inverse of the local hydraulic impedance $z(s) = y^{-1}$. As for the electrical description, the integral of relations (6) and (10) along the curvilinear centerline arc length s of the aqueduct provides the total hydraulic admittance Y of the aqueduct relating the flux Q_U to the pressure difference ΔP . Considering the flux $Q_U = -y_U(s)K_U(s)e^{it} = -\tilde{Q}_U e^{it}$ with the amplitude

$$\tilde{Q}_U = -y_U(s)K_U(s)$$

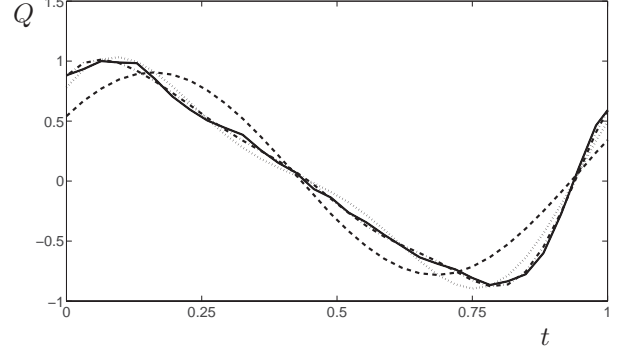


Fig. 6. Solid line: MRI nondimensional flux versus times (over a cardiac cycle). dashed, dotted, and dot-dashed lines: reconstructed flux with $n = 1, 2,$ and $3,$ respectively (Patient D).

leads to

$$\int \frac{\tilde{Q}_U}{y_U(s)} ds = - \int K_U(s) ds = \Delta P_U \quad (14)$$

\tilde{Q}_U is constant along the aqueduct (incompressible Newtonian fluid) such that

$$\tilde{Q}_U = Y \Delta P_U = \frac{1}{\int_0^L y_U(s)^{-1} ds} \Delta P_U \quad (15)$$

where ΔP_U is the pressure difference obtained between the two extremities of the aqueduct of length L for a flux amplitude \tilde{Q}_U . A discrete version of (15) over each successive ellipses Ω_i has been implemented with finite-difference integration. This was done for each mode k to evaluate the admittance Y^k of each flux Q_U^k . The real and imaginary components of $Y^k = C^k + iS_c^k$ are called conductance and susceptance, respectively. The resulting complex admittance results are discussed in the next section. We also evaluate the complex impedance $Z^k = \frac{1}{Y^k}$ and find that, for all patients, $\Im(Z^k) > 0$. Thus, the electric model of the aqueduct is a self-inductance with $Z^k = R^k + L^k \omega^k i$ with a phase lag $\phi^k = \tan^{-1}(\frac{L^k \omega^k}{R^k})$. Using the truncation to the first three modes, described in the previous section, leads to the reconstruction of the total pressure drop for the aqueduct

$$\Delta P = \left(R^0 Q_S + \sum_{k=1}^3 \Re(Z^k \tilde{Q}_U^k e^{i\omega^k t}) \right), \quad (16)$$

which is the main contribution to the TRP drop, i.e., $\Delta P \approx \text{TRP}$, as will be discussed in Section III. The values of Q_S , \tilde{Q}_U^k , R^k , and L^k are reported in Table II.

D. Discussion of the Model's Validity

In this section, we investigate the validity of the creeping flow regime that has been developed for CSF in the previous sections. As mentioned in Section I, many detailed studies [16]–[20], [26] have already investigated moderate Reynolds number flow in curved pipes. In this context, inertial and curvature effects are properly described by a single dimensionless Dean number $De = Re \cdot \sqrt{\lambda}$ for stationary flows or by a reduced Reynolds number $Re_s = (Re/\alpha)^2 \lambda$ for oscillating flows. The latter parameter Re_s is generally small (see Table III) in the normal

TABLE II
TABLE OF NUMERICAL VALUES MEASURED FOR THREE DIFFERENT PATIENTS

	Patient D	Patient E	Patient F
λ	0.18	0.25	0.12
e	0.91	0.92	0.86
m	0.68	0.68	0.59
Re	5.78	21.01	16.60
De	2.49	10.52	5.87
Re_s	0.043	0.753	0.35
\bar{a} mm	4.21	4.45	3.54
L mm	14.22	9.85	9.3
Q_{max} mm ³ /s	99	371	254
Q_S mm ³ /s	6	5	3
\bar{Q}_U^1 mm ³ /s	84	322	203
\bar{Q}_U^2 mm ³ /s	26	49	58
\bar{Q}_U^3 mm ³ /s	9	56	8
u_{max} mm/s	9.08	21.28	34.24
τ_{usmax}	1.22	0.30	0.27
τ_{uumax}	3.83	8.02	1.32
$\sqrt{ab_{min}}$ mm	1.71	2.19	1.37
α^1 (f ¹ Hz)	12.00 (1.42)	12.14 (1.30)	9.87 (1.36)
α^2 (f ² Hz)	16.97 (2.84)	17.16 (2.60)	13.96 (2.71)
α^3 (f ³ Hz)	20.78 (4.26)	21.02 (3.90)	17.10 (4.07)
R^0	61.1	34.2	37.0
$(R^1; L^1)$	(77.7; 23.8)	(48.1; 19.7)	(45.7; 13.6)
$(R^2; L^2)$	(97.2; 22.5)	(63.2; 20.1)	(56.7; 13.2)
$(R^3; L^3)$	(114; 22.8)	(72.8; 18.9)	(64.6; 12.4)
ϕ^1	69°	73°	68°
ΔP_{max} Pa	1.76	2.43	2.64

Where units are not stated, the quantity is dimensionless. The resistances R^k are nondimensionalized by $\mu L/\bar{a}^4$ with $k = 0, 1, 2, 3$ and the inductances L^k by $\mu L/\bar{a}^4 \omega^k$ with $k = 1, 2, 3$, with $\omega^k = 2\pi f^k$.

conditions considered, so that it is reasonable to neglect inertial corrections to the leading order viscous contributions. Most studies have focused on the occurrence and structure of secondary transverse counterrotating flows arising from the conjugated effects of inertia and curvature. Systematic Dean number and reduced Reynolds number expansions, respectively, are proposed for those corrections [16]–[20], [26]. Here, we are mainly interested in the leading order viscous contribution to the flux for a given longitudinal pressure gradient.

Following previous authors, we looked for the leading order flow description in the range of the fluid flow parameters evaluated by MRI (see, for example, Table II). According to [17] and [18], small reduced Reynolds number $Re_s \approx 1$ (see Table III for the mean value of Re_s) allows us to assume that the CSF flow is well approximated by (3). Moreover, the pressure/flux relationship in a curved pipe with an elliptical cross section has been thoughtfully analyzed in [20], where inertial deviations from the stationary creeping flow regime are systematically provided for each family of parameter $m = \sqrt{(a-b)/(a+b)}$, Reynolds number Re , and dimensionless curvature λ

$$E = \lambda^2 (A(m) + B(m)Re^2 + C(m)Re^4) \quad (17)$$

where coefficients $A(m)$, $B(m)$, and $C(m)$ can be extracted from figures given in [20]. E is the dimensionless relative difference (the relative error) between the creeping flow flux and the real flux, which includes inertial effects up to third-order corrections that are valid for Reynolds numbers as large as 1000. This relation provides an explicit quantitative test for the validity

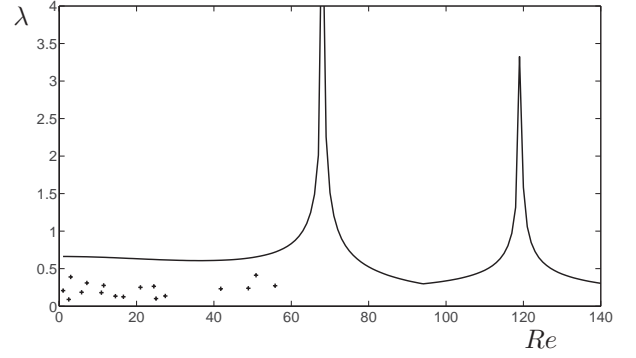


Fig. 7. Plot of λ versus the Reynolds number Re for $0.57 < m < 0.70$. Validity of the low Dean number approximation. Lines correspond to $E = 10\%$ error on the TRP and are plotted for $A(m) = -0.22$, $B(m) = -6 \cdot 10^{-5}$, $C(m) = 2 \cdot 10^{-8}$ ($m = 0.54$) and for $A(m) = 3.12$, $B(m) = -2 \cdot 10^{-4}$, $C(m) = 10^{-9}$ ($m = 0.57$). Each cross (+) corresponds to a patient measurement.

of our approximation, which we have illustrated in Fig. 7. Furthermore, this formula also gives an index for testing how good the proposed approximation is in certain diseases for which the Reynolds number might be large, or the aspect ratio λ might not be small. This can be done using the parameters $A(m)$, $B(m)$, and $C(m)$ provided in the legend of Fig. 7.

Using $E = 0.1$ when looking for an approximation to the flux with an error of $< 10\%$, relation (17) provides a curve in the (λ, Re) plane for comparison. Most of patients (17 out of 20) had an ellipticity m between 0.57 and 0.70, so we chose the appropriate value of m for parameters $A(m)$, $B(m)$, and $C(m)$ to compute the validity curve represented by the black line in Fig. 7. All the experimental data points lie below the 10% error curve, which indicates that our approximation for the linear pressure/flux relationship is accurate to within 10%. Since the mode truncation described in the previous section leaves out 15% of the total flow, the linear viscous approximation is more than a consistent approximation in this context. Thus, the validity of the approximation used in this paper compares well with the real physiological condition of the pool of patient considered.

III. RESULTS AND DISCUSSION

The very slight pressure variations observed in ventricles (lateral, third, and fourth) together with the pressure variations observed inside the cerebral aqueduct in the full CVD simulations illustrated in [12], Fig. 5] demonstrate the validity of the key hypothesis of our study: most of the pressure variations between LVs and spinal subarachnoid spaces arise within the thin passage of the cerebral aqueduct. Hence, the pressure difference amplitude obtained, of a few pascals, which is compatible with the TRP obtained in [12], is another confirmation that this hypothesis is relevant (see Fig. 8). Entrance effects discussed in [27] and numerically observed in [5] are expected to be small when considering realistic anatomical reconstruction of the cerebral aqueduct having a gently varying diameter.

As mentioned in [10], the hydrodynamic pressure, which can be reconstructed by solving CSF equations, is defined up to an unprescribed constant. In order to discuss our result quantitatively, it is interesting to consider how the cerebral aqueduct

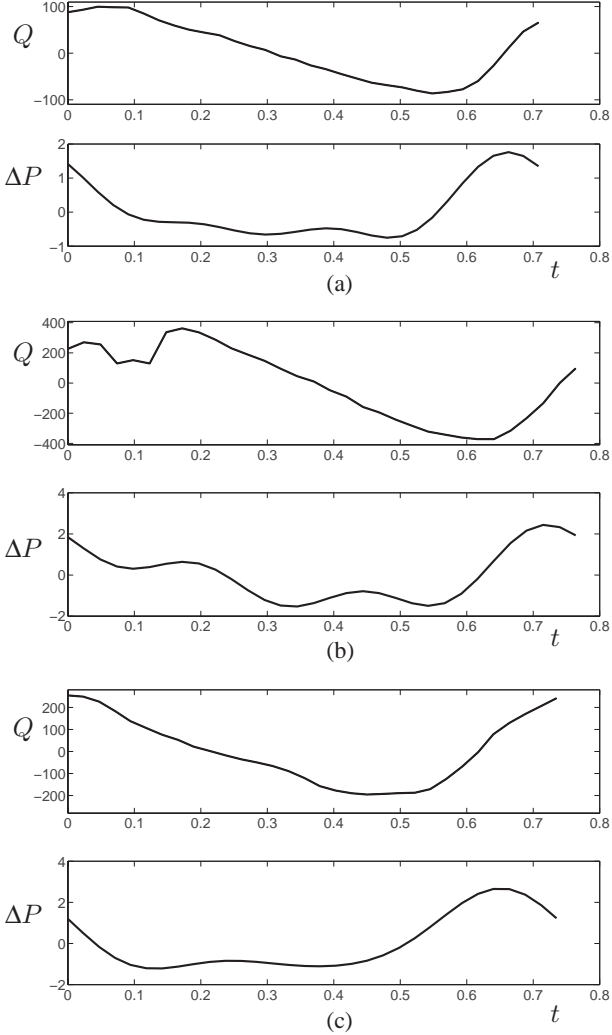


Fig. 8. (Top) experimental flux Q in $\text{mm}^3 \cdot \text{s}^{-1}$. (Bottom) Reconstructed oscillating pressure ΔP in pascals for a cardiac cycle in seconds.

fits into a more global intracranial pressure distribution model. The electrical model depicted in Fig. 9 is very close to those proposed in [7] and [28]. This linear model is easy to solve for the intracranial pressure P_{ICP}

$$P_{ICP} = \frac{RP_{V3} + RZ^1 C \omega^1 i P_0 + Z^1 P_{SAS}}{R + RZ^1 C \omega^1 i + Z^1} \quad (18)$$

and thus evaluation of aqueduct impedance parameters Z^1 is useful but not sufficient to determine intracranial pressure. This conclusion is similar to the one drawn by previous authors [29], who pointed out that cine phase-contrast MRI combined with fluid-pressure flow evaluation cannot provide intrinsic pressure values but necessitates supplementary information such as estimation of compliance and/or monitoring [30].

Nevertheless, a positive correlation between TRP and ICP increase has been recognized [31], [32], so the evaluation of TRP is also interesting. As mentioned in Section I, the cerebral aqueduct is the main contributor to the total resistance between LVs and SAS. As $R^1 \gg R$, using the electrical model of Fig. 9, a good approximation of P_{TRP} is

$$P_{TRP} = P_{V3} - P_{SAS} \approx P_{V3} - P_{ICP}. \quad (19)$$

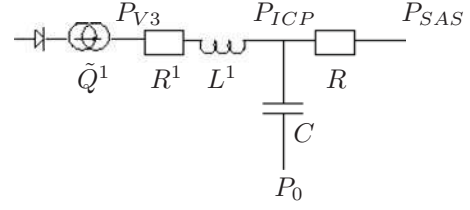


Fig. 9. Electrical model representing CSF flow.

TABLE III
TABLE OF NUMERICAL MEAN VALUES MEASURED FOR 20 DIFFERENT PATIENTS, WITH STANDARD DEVIATION

λ	0.19 ± 0.06
e	0.84 ± 0.14
m	0.59 ± 0.14
Re	29 ± 25
De	14 ± 13
Re_s	0.49 ± 0.62
\bar{a} mm	3.6 ± 0.9
L mm	10.2 ± 2.7
Q_{max} mm^3/s	357 ± 290
Q_S mm^3/s	9.1 ± 13
\bar{Q}_U^1 mm^3/s	270 ± 247
\bar{Q}_U^2 mm^3/s	67 ± 46
\bar{Q}_U^3 mm^3/s	25 ± 20
u_{max} mm/s	32 ± 25
τ_{usmax}	1.7 ± 2.2
$\tau_{uu_{max}}$	5 ± 6.4
\sqrt{ab}_{min} mm	1.59 ± 0.3
α^1 (f^1 Hz)	9.5 ± 2.2 (1.2 ± 0.2)
α^2 (f^2 Hz)	13.7 ± 3.1 (2.5 ± 0.45)
α^3 (f^3 Hz)	17 ± 3.8 (4 ± 0.8)
R^0	32 ± 20 ($2.2 \pm 1.55 \cdot 10^6 \text{ Pa} \cdot \text{s} \cdot \text{m}^3$)
R^1	41.3 ± 27.1 ($2.7 \pm 1.7 \cdot 10^6 \text{ Pa} \cdot \text{s} \cdot \text{m}^3$)
L^1	14.9 ± 10.5 ($7.64 \pm 4 \cdot 10^5 \text{ Pa} \cdot \text{s}^2 \cdot \text{m}^3$)
R^2	51.9 ± 34.3 ($3.5 \pm 2.1 \cdot 10^6 \text{ Pa} \cdot \text{s} \cdot \text{m}^3$)
L^2	14.4 ± 10.1 ($3.5 \pm 1.7 \cdot 10^5 \text{ Pa} \cdot \text{s}^2 \cdot \text{m}^3$)
R^3	60.3 ± 40 ($4 \pm 2.4 \cdot 10^6 \text{ Pa} \cdot \text{s} \cdot \text{m}^3$)
L^3	14.1 ± 10 ($2.3 \pm 1.3 \cdot 10^5 \text{ Pa} \cdot \text{s}^2 \cdot \text{m}^3$)
ϕ^1	$63^\circ \pm 7^\circ$
ΔP_{max} Pa	4.316 ± 3.6
ΔP_S Pa	0.039 ± 0.029

Hence, from an evaluation of the pressure drop between the third and fourth ventricles $P_{V3} - P_{ICP}$, this simple electrical model leads to the conclusion that it is possible to obtain a good approximation for the TRP drop $P_{TRP} = P_{V3} - P_{SAS}$, and noninvasive estimation of this pressure from cine phase-contrast MRI is thus possible.

We found a TRP magnitude of 4.3 ± 3.6 Pa and a mean TRP of 0.039 ± 0.029 Pa (respectively, ΔP_{max} and ΔP_S in Table III) which can be compared with typical literature values. *In vivo* studies on dogs with kaolin-induced hydrocephalus [33] report a mean TRP of 34 Pa. In the cat kaolin model, Shapiro *et al.* [34] found zero mean TRP. More recently, Penn *et al.* [35] have found that the mean TRP in dogs was not greater than

the resolution of their sensors (66 Pa), and consequently, they concluded that the magnitude of such gradients could not be accurately determined in their study. A clinical study has been performed by Stephensen *et al.* [36] on ten human patients having communicating or noncommunicating hydrocephalus. The first microsensor was placed in the ventricle system, inside a ventricular catheter, and the second one in the subarachnoid space. When using a temporal average, they found a mean TRP of 1.3 ± 32 Pa, while the deviation from this temporal TRP pressure data (which should be related to the amplitude of TRP pressure oscillation) could be evaluated at 65 ± 22 Pa from their Fig. 3. The mean TRP value reported in [36] was compared to our stationary TRP ΔP_S using a Mann–Whitney test. We found no significant difference with a p-value of 0.9 (nonparametric tests are insensitive to inhomogeneity of variance that may result from the use of different measurement methods). Nevertheless, when comparing the ten temporal standard deviations reported in [36] with ΔP_{\max} of our 20 healthy patients, we found them significantly different, with a p-value smaller than 10^{-3} , which is consistent with the large departure from the statistical mean (65 Pa, as against, our 4.3 Pa). This difference between normal and pathological situations, and average value obtained for the oscillating part of the TRP, are also consistent with other estimates obtained from cine MRI measurements, 3-D reconstruction of brain geometry, and direct simulation by Penn [37]. They report a TRP magnitude below 10 Pa for healthy volunteers and close to 50 Pa in patients with hydrocephalus. The ICP in normal subjects is of the order of 500 Pa and the TRP smaller than 10 Pa. In abnormal conditions, the ICP can become as high as 3000 Pa, whereas the TRP does not exceed 30 Pa [10]. Our findings are thus consistent with all these considerations related to previous measurements. Furthermore, it is important to stress that previous direct experimental measurements of the TRP were obtained by evaluating pressure differences that were 10–100 times smaller than the actual value measured. As the resolution of the sensors was hardly a hundred times smaller than the actual measurement, the reliability of the direct measurements can be called into question. One major contribution of our TRP evaluation, apart from its painless and noninvasive nature, lies in the fact that it is much more precise since the limitation is related to the evaluated flux and, to a lesser extent, the spatial resolution of the reconstructed aqueduct.

Another consequence of our findings is to show that the stationary Hagen–Poiseuille approximation for the aqueduct flow used in [8] and [38] has to be corrected. Our results show that the leading order contribution comes from the first oscillatory mode $k = 1$, for which the Womersley number is nonzero, and thus, the resulting admittance is complex (see Fig. 10). Analytical result (11) (derived from [24]) is fully consistent with finite-element numerical evaluation, as represented in Fig. 10, where the two curves cannot be distinguished. Furthermore, our evaluation shows that the resistance part R^k does not predominate over the inductance part L^k . Our results (see Tables II and III) show an average phase lag ϕ^1 of $63 \pm 7^\circ$ between pressure and flow, which is consistent with the 58° found in [12] using 3-D numerical simulations. We also note the influence of α

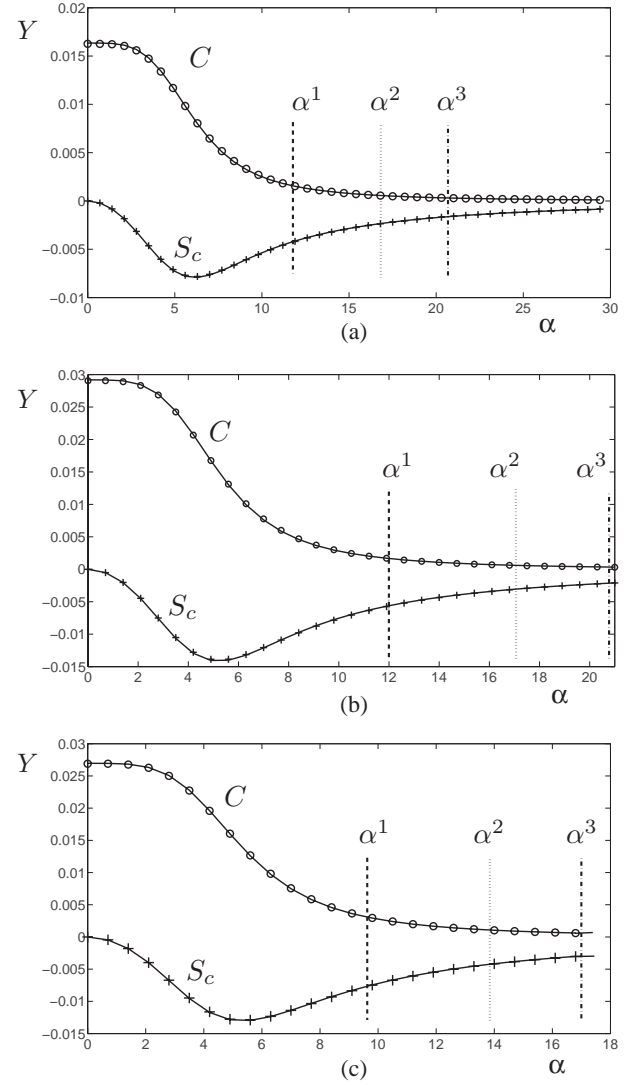


Fig. 10. Hydraulic admittance $Y = C + iS_c$ versus Womersley number α . The hydraulic conductance $C(\alpha)$ is shown as a solid line, and the susceptance $S_c(\alpha)$ as a dashed line. The vertical lines indicate the Womersley numbers α^k for $k = 1$, $k = 2$, and $k = 3$.

on the electric impedance. When α^1 is three times larger, the electric resistance and inductance are five and ten times larger, respectively. The mean values of R^1 and L^1 over the 20 patients are given in Table III.

Finally, it is also interesting to note that our findings might contribute to the understanding of pathological evolutions associated with aqueduct stenosis, which is a common cause of hydrocephalus. Such stenosis increases wall shear stresses and can be easily detected by our method. Increased wall shear stresses occur with increased pressure drop and may result in ongoing damage to the aqueduct where the area of the sections is minimal, as mentioned in [15]. This effect is also observed in healthy patients in Fig. 11(a)–(c) where the maximum for the total wall shear stress of nonstationary flow components τ_U is shown to be maximal when the local section πab is minimal.

APPENDIX

This section provides a detailed derivation of the wall shear stress relations (8), (9), (12), and (13). Let us call the total velocity field \mathbf{U} . Due to the low-curvature geometry of the aqueduct and the incompressibility condition, \mathbf{U} can be decomposed into a leading order term in the local longitudinal direction, ut , plus a small correction $\lambda \mathbf{v}$ for the in-plane contribution in the elliptic section $\Omega(s)$, where $\mathbf{v} \sim O(1)$, with $\lambda \ll 1$ and $\mathbf{v} \cdot \mathbf{t} = 0$, so that

$$\mathbf{U} = ut + \lambda \mathbf{v}.$$

From the chosen nondimensionalization, the in-plane coordinates (x, y) in section $\Omega(s)$ are scaled by a and the longitudinal coordinate z by R_c , so that the local dimensionless gradient operator reads $\nabla = (\nabla_2, \lambda \partial_z)$, where $\nabla_2 = (\partial_x, \partial_y)$. The dimensionless stress tensor σ then reads

$$\sigma = -p + \frac{\lambda}{2} (\nabla \otimes \mathbf{U} + \nabla^T \otimes \mathbf{U})$$

where we have consistently used the viscous pressure $(\mu UL/\bar{a}^2)$ to define the dimensionless stress σ , such that $\sigma^* = (\mu UL/\bar{a}^2)\sigma$. By considering only the deviatoric part of the stress σ_d , (since the viscous stress is the only contribution to the shear here)

$$\sigma_d = \lambda \nabla_2 \otimes ut + O(\lambda^2) = \lambda \begin{pmatrix} 0 & 0 & \frac{\partial u}{\partial x} \\ 0 & 0 & \frac{\partial u}{\partial y} \\ \frac{\partial u}{\partial x} & \frac{\partial u}{\partial y} & 0 \end{pmatrix} + O(\lambda^2)$$

we then compute the local shear stress τ (a scalar), at each point of the wall $\partial\Omega$ where the normal in-plane vector is denoted \mathbf{n}

$$\tau = \mathbf{t} \cdot \sigma_d \cdot \mathbf{n} = \lambda \nabla_2 u \cdot \mathbf{n} + O(\lambda^2).$$

In the following, we neglect $O(\lambda^2)$ terms and no longer mention them. In the stationary case, as given in (5), u can be computed analytically, and we have

$$\tau_S = \frac{\lambda}{4} \frac{a^2 b^2}{a^2 + b^2} K_S(s) \mathbf{t} \cdot \begin{pmatrix} 0 & 0 & \frac{2x}{a^2} \\ 0 & 0 & \frac{2y}{b^2} \\ \frac{2x}{a^2} & \frac{2y}{b^2} & 0 \end{pmatrix} \cdot \mathbf{n}$$

while

$$\mathbf{n} = \frac{1}{\sqrt{\frac{4x^2}{a^4} + \frac{4y^2}{b^4}}} \begin{pmatrix} \frac{2x}{a^2} \\ \frac{2y}{b^2} \\ 0 \end{pmatrix}$$

and we thus obtain result (8)

$$\tau_S = \lambda \frac{a^2 b^2}{a^2 + b^2} \sqrt{\frac{x^2}{a^4} + \frac{y^2}{b^4}} K_S(s).$$

Furthermore, we can estimate the total wall shear stress by integrating along the contour $\partial\Omega$

$$\tau_T = \lambda \left(\int_{\partial\Omega} \nabla_2 u \cdot \mathbf{n} dl \right)$$

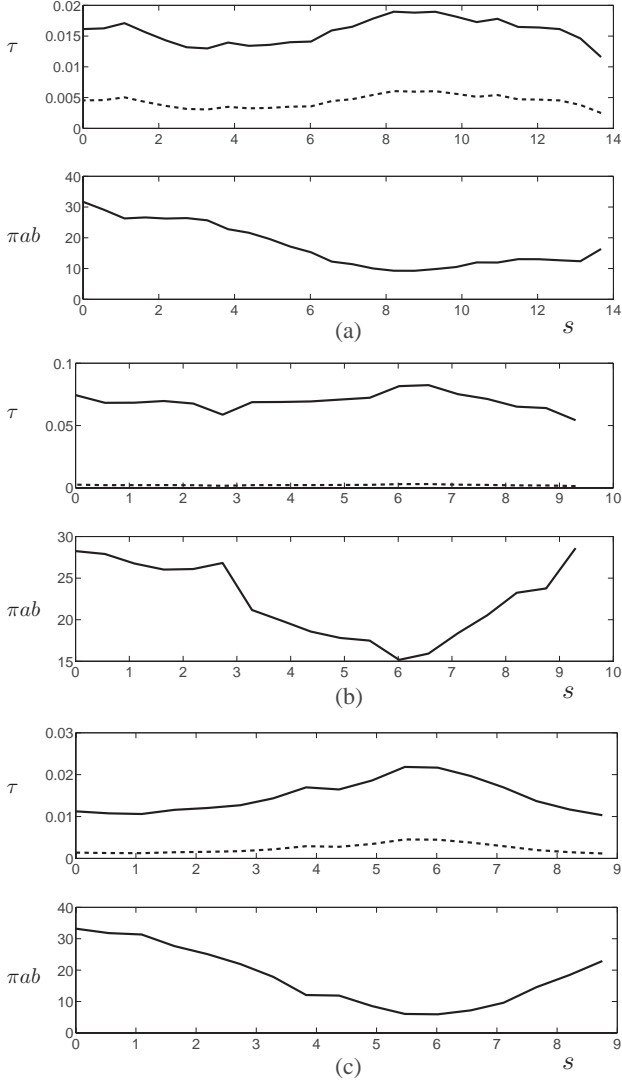


Fig. 11. (Top) Oscillating (solid line) τ_{TU} and stationary (dashed line) τ_{TS} wall shear stress in pascals. (Bottom) Surface area $\pi a(s)b(s)$ in mm^2 of the aqueduct section versus curvilinear coordinate s .

IV. CONCLUSION

Our contribution has successfully tested the validity of a low curvature/low reduced Reynolds number approximation for CSF flow in real patients. Using this approximation, we propose a simple and very fast method for evaluating the aqueduct admittance from MRI anatomical images and cine acquisitions. This method can also evaluate the shear stress within the cerebral aqueduct, which is greatest in its smallest portion. The proposed approach provides the total pressure drop in the aqueduct, which permits a simple, noninvasive patient-based, approximate evaluation of the TRP.

Combined with other invasive (e.g., intrathecal pressure monitoring) or noninvasive (compliance estimation [9], [29], [39]) measurements, our method could be useful for estimating intracranial pressure or evaluating a patient's disorder.

which, from the Green formula also reads

$$\tau_T = \lambda \int_{\Omega} \nabla^2 u \, dS \quad (20)$$

where we have used the same notation $\nabla^2 = \partial_x^2 + \partial_y^2$ as in (3). If we use (3) in the stationary case, this leads to relation (9)

$$\tau_{TS} = \lambda \left(-K_S \int_{\Omega} dS \right) = -\lambda \pi ab K_S.$$

Alternatively, using (3) in the unstationary case leads to the complex version of (12)

$$\tau_{TU} = \lambda \left(-i\alpha^2 \tilde{Q}_U - \pi ab K_U \right) e^{it}.$$

REFERENCES

- [1] O. Balédent, C. Gondry-Jouet, M.-E. Meyer, G. D. Marco, D. L. Gars, M.-C. Henry-Feugeas, and I. Idy-Peretti, "Relationship between cerebrospinal fluid and blood dynamics in healthy volunteers and patients with communicating hydrocephalus," *Investigative Radiol.*, vol. 39, pp. 45–55, 2004.
- [2] S. Stoquart-Elsankari, O. Balédent, C. Gondry-Jouet, M. Makki, O. Godefroy, and M.-E. Meyer, "Aging effects on cerebral blood and cerebrospinal fluid flows," *J. Cerebral Blood Flow Metabolism: Official J. Int. Soc. Cerebral Blood Flow Metabolism*, vol. 27, no. 9, pp. 1563–1572, Sep. 2007.
- [3] R. Tain and N. Alperin, "Compliance effect on amplitude and phase of cranio-spinal CSF Flow Measured by MRI," in *Proc. 3rd Int. Conf. Bioinform. Biomed. Eng.*, 2009, pp. 1–4.
- [4] M. Ursino, "A mathematical study of human intracranial hydrodynamics part i—The cerebrospinal fluid pulse pressure," *Ann. Biomed. Eng.*, vol. 16, no. 30, pp. 379–401, 1988.
- [5] L. Fin and R. Grebe, "Three dimensional modeling of the cerebrospinal fluid dynamics and brain interactions in the aqueduct of sylvius," *Comput. Methods Biomech. Biomed. Eng.*, vol. 6, no. 3, pp. 163–70, Jun. 2003.
- [6] K. Ambarki, O. Baledent, G. Kongolo, R. Bouzerar, S. Fall, and M.-E. Meyer, "A new lumped-parameter model of cerebrospinal hydrodynamics during the cardiac cycle in healthy volunteers," *IEEE Trans. Biomed. Eng.*, vol. 54, no. 3, pp. 483–491, Mar. 2007.
- [7] A. Linninger, M. Xenos, B. Sweetman, S. Ponskhe, X. Guo, and R. Penn, "A mathematical model of blood, cerebrospinal fluid and brain dynamics," *J. Math. Biol.*, vol. 59, no. 6, pp. 729–759, 2009.
- [8] N. Masoumi, D. Bastani, S. Najarian, F. Ganji, F. Farmanzad, and A. S. Seddighi, "Mathematical modeling of CSF pulsatile hydrodynamics based on fluid-solid interaction," *IEEE Trans. Biomed. Eng.*, vol. 57, no. 6, pp. 1255–63, Jun. 2010.
- [9] B. Cohen, A. Voorhees, S. Vedel, and T. Wei, "Development of a theoretical framework for analyzing cerebrospinal fluid dynamics," *Cerebrospinal Fluid Res.*, vol. 6, p. 12, Jan. 2009.
- [10] A. A. Linninger, M. Xenos, D. C. Zhu, M. R. Somayaji, S. Kondapalli, and R. D. Penn, "Cerebrospinal fluid flow in the normal and hydrocephalic human brain," *IEEE Trans. Biomed. Eng.*, vol. 54, no. 2, pp. 291–302, Feb. 2007.
- [11] V. Kurtcuoglu, M. Soellinger, P. Summers, K. Boomsma, D. Poulidakos, P. Boesiger, and Y. Ventikos, "Computational investigation of subject-specific cerebrospinal fluid flow in the third ventricle and aqueduct of Sylvius," *J. Biomech.*, vol. 40, no. 6, pp. 1235–1245, Jan. 2007.
- [12] B. Sweetman, M. Xenos, L. Zitella, and A. A. Linninger, "Three-dimensional computational prediction of cerebrospinal fluid flow in the human brain," *Comput. Biol. Med.*, vol. 41, no. 2, pp. 67–75, Feb. 2011.
- [13] R. Penn, S. Basati, B. Sweetman, X. Guo, and A. Linninger, "Ventricular wall movements and cerebrospinal fluid flow in hydrocephalus," *J. Neurosurg.*, vol. 115, pp. 159–164, 2011.
- [14] C. Johanson, J. Duncan, P. Klinge, T. Brinker, E. Stopa, and G. Silverberg, "Multiplicity of cerebrospinal fluid functions: New challenges in health and disease," *Cerebrospinal Fluid Res.*, vol. 5, 2008.
- [15] E. E. Jacobson, D. F. Fletcher, M. K. Morgan, and I. H. Johnston, "Computer modelling of the cerebrospinal fluid flow dynamics of aqueduct stenosis," *Med. & Biol. Eng. & Comput.*, vol. 37, no. 1, pp. 59–63, Jan. 1999.
- [16] W. Lyne, "Unsteady viscous flow in a curved pipe," *J. Fluid Mech.*, vol. 45, no. part 1, pp. 13–31, 1971.
- [17] R. Zalosh and W. Nelson, "Pulsating flow in a curved tube," *J. Fluid Mech.*, vol. 59, no. 04, pp. 693–705, 1973.
- [18] D. Gammack and P. Hydon, "Flow in pipes with non-uniform curvature and torsion," *J. Fluid Mech.*, vol. 433, no. 1, pp. 357–382, 2001.
- [19] H. Topakoglu and M. Ebadian, "On the steady laminar flow of an incompressible viscous fluid in a curved pipe of elliptical cross-section," *J. Fluid Mech.*, vol. 158, no. 1, pp. 329–340, Apr. 1985.
- [20] H. Topakoglu and M. Ebadian, "Viscous laminar flow in a curved pipe of elliptical cross-section," *J. Fluid Mech.*, vol. 184, no. 1, pp. 571–580, 1987.
- [21] O. Balédent, M.-C. Henry-Feugeas, and I. Idy-Peretti, "Cerebrospinal fluid dynamics and relation with blood flow : a magnetic resonance study with semiautomated cerebrospinal fluid segmentation," *Investig. Radiol.*, vol. 36, pp. 368–377, 2001.
- [22] B. R. Robertson, U. Kohler, P. R. Hoskins, and I. Marshall, "Flow in elliptical vessels calculated for a physiological waveform," *J. Vascular Res.*, vol. 38, pp. 73–82, 2001.
- [23] E. M. Mejdí Azaïez and M. Deville, *Eléments Finis Pour Les Fluides Incompressibles*. Lausanne, Switzerland: Presses polytechniques, 2012.
- [24] M. Haslam and M. Zamir, "Pulsatile flow in tubes of elliptical cross sections," *Ann. Biomed. Eng.*, vol. 26, no. 5, pp. 780–787, 1998.
- [25] T. Huang, H. Chung, M. Chen, and L. Giiang, "Supratentorial cerebrospinal fluid production rate in healthy adults: Quantification with two-dimensional cine phase-contrast MR imaging with high temporal and spatial resolution," *Radiology*, vol. 233, pp. 603–608, 2004.
- [26] W. R. Dean and J. M. Hurst, "Note on the motion of a fluid in a curved pipe," *Phil. Mag.*, vol. 7, pp. 208–223, 1927.
- [27] L. Talbot and K. Gong, "Pulsatile entrance flow in a curved pipe," *J. Fluid Mech.*, vol. 127, pp. 1–25, 1983.
- [28] Z. H. Czosnyka, K. Cieslicki, M. Czosnyka, and J. D. Pickard, "Hydrocephalus shunts and waves of intracranial pressure," *Med. & Biol. Eng. & Comput.*, vol. 43, no. 1, pp. 71–77, Jan. 2005.
- [29] N. Alperin, S. Lee, F. Loth, P. Raksin, and T. Lichtor, "MR-intracranial pressure (ICP): A method to measure intracranial elastance and pressure noninvasively by means of MR imaging: Baboon and human study1," *Radiology*, vol. 217, no. 3, pp. 877–885, 2000.
- [30] M. Czosnyka, L. Steiner, M. Balestreri, P. Schmidt, E. and. Smielewski, P. Hutchinson, and J. Pickard, "Concept of true ICP in monitoring and prognostication in head trauma," *Acta Neurochir suppl*, vol. 95, no. 341, pp. 1–4, 2005.
- [31] E. S. Conner, L. Foley, and P. M. L. Black, "Experimental normal-pressure hydrocephalus is accompanied by increased transmantle pressure," *J. Neurosurg.*, vol. 61, pp. 322–327, 1984.
- [32] H. Hoff and R. Barber, "Transcerebral mantle pressure in normal pressure hydrocephalus," *Arch. Neurol.*, vol. 31, pp. 101–105, 1974.
- [33] E. Conner, L. Foley, and P. Black, "Experimental normal-pressure hydrocephalus is accompanied by increased transmantle pressure," *J. Neurosurg.*, vol. 61, pp. 322–327, 1984.
- [34] K. Shapiro, I. Kohn, F. Takei, and C. Zee, "Progressive ventricular enlargement in cats in the absence of transmantle pressure gradients," *J. Neurosurg.*, vol. 67, pp. 88–92, 1987.
- [35] R. Penn, M. Lee, A. Linninger, K. Miesel, S. Lu, and L. Stylos, "Pressure gradients in the brain in an experimental model of hydrocephalus," *J. Neurosurg.*, vol. 102, pp. 1069–1075, 2005.
- [36] H. Stephensen, M. Tisell, and C. Wikkelso, "There is no transmantle pressure gradient in communicating or noncommunicating hydrocephalus," *Neurosurgery*, vol. 50, pp. 763–773, 2002.
- [37] R. Penn, "Neurosurgical forum: Letters to the editor," *J. Neurosurg.*, vol. 104, pp. 986–995, 2006.
- [38] A. Smillie, I. Sobey, and Z. Molnar, "A hydroelastic model of hydrocephalus," *J. Fluid Mech.*, vol. 539, no. 1, pp. 417–443, 2005.
- [39] R.-W. Tain and N. Alperin, "Noninvasive intracranial compliance from MRI-based measurements of transcranial blood and CSF flows: Indirect versus direct approach," *IEEE Trans. Biomed. Eng.*, vol. 56, no. 3, pp. 544–551, Mar. 2009.